Biophysical Journal
Article

Biophysical Society

Characterizing Conduction Channels in Postinfarction Patients Using a Personalized Virtual Heart

Dongdong Deng,[1,2] Adityo Prakosa,[2] Julie Shade,[2] Plamen Nikolov,[2] and Natalia A. Trayanova[2,*]
[1]School of Biomedical Engineering, Dalian University of Technology, Dalian, Liaoning, China and [2]Department of Biomedical Engineering, Johns Hopkins University, Baltimore, Maryland

ABSTRACT Patients with myocardial infarction have an abundance of conduction channels (CC); however, only a small subset of these CCs sustain ventricular tachycardia (VT). Identifying these critical CCs (CCCs) in the clinic so that they can be targeted by ablation remains a significant challenge. The objective of this study is to use a personalized virtual-heart approach to conduct a three-dimensional (3D) assessment of CCCs sustaining VTs of different morphologies in these patients, to investigate their 3D structural features, and to determine the optimal ablation strategy for each VT. To achieve these goals, ventricular models were constructed from contrast enhanced magnetic resonance imagings of six postinfarction patients. Rapid pacing induced VTs in each model. CCCs that sustained different VT morphologies were identified. CCCs' 3D structure and type and the resulting rotational electrical activity were examined. Ablation was performed at the optimal part of each CCC, aiming to terminate each VT with a minimal lesion size. Predicted ablation locations were compared to clinical. Analyzing the simulation results, we found that the observed VTs in each patient model were sustained by a limited number (2.7 $\pm$ 1.2) of CCCs. Further, we identified three types of CCCs sustaining VTs: I-type and T-type channels, with all channel branches bounded by scar, and functional reentry channels, which were fully or partially bounded by conduction block surfaces. The different types of CCCs accounted for 43.8, 18.8, and 37.4% of all CCCs, respectively. The mean narrowest width of CCCs or a branch of CCC was 9.7 $\pm$ 3.6 mm. Ablation of the narrowest part of each CCC was sufficient to terminate VT. Our results demonstrate that a personalized virtual-heart approach can determine the possible VT morphologies in each patient and identify the CCCs that sustain reentry. The approach can aid clinicians in identifying accurately the optimal VT ablation targets in postinfarction patients.

SIGNIFICANCE This article presents an insight into human infarct-related ventricular tachycardia (VT) by providing information regarding the organization and structure of critical conduction channels (CCCs) that sustain VT and how the different types of CCCs determine VT morphology. The simulation results demonstrate that purely anatomical reentries as well as reentries with a functional component could give rise to infarct-related VT in patients. As the ablation targets predicted in our models are consistent with the ablation lesions executed in the clinic, the current study underscores the potential of patient-specific models to identify offline, before the procedure, the CCCs which sustain reentry thus helping to guide the clinical procedure.

INTRODUCTION

Ventricular tachycardia (VT), a life-threatening fast heart rhythm, occurs frequently in patients with prior myocardial infarction (MI) and can lead to sudden cardiac death. Clinical and experimental studies show that VT is often caused by a reentrant wave traveling through an isthmus within the infarcted area, commonly known as a conduction channel (CC) (1–5). Patients with MI have an abundance of CCs, but only a small subset of CCs sustain reentry (1,3). CCs that sustain reentry are the primary target for VT ablation in the clinic (1,4,5). However, identifying which CCs sustain reentry remains a significant challenge for several reasons, including insufficient spatial resolution to identify critical VT propagation pathways by electroanatomic mapping (6–8) and ambiguities in correlating electrical maps with heart anatomy and infarct structure (9). Furthermore, as a recent high-resolution study of infarct-related VTs in

Submitted February 25, 2019, and accepted for publication July 10, 2019.
*Correspondence: ntrayanova@jhu.edu
Editor: Daniel Beard.
https://doi.org/10.1016/j.bpj.2019.07.024

ex vivo hearts demonstrated (10), reentrant waves through the zone of infarct could be established through complex three-dimensional (3D) pathways, which may be difficult to reconstruct by mapping the ventricular surfaces only (5,11,12).

Recent advances in noninvasive imaging techniques have shown promise in supplementing the information gained from electrophysiology studies by providing detail regarding the structural remodeling in MI (13,14). In particular, clinical late gadolinium-enhanced (LGE) magnetic resonance imaging (MRI) has become the gold standard for assessing the location, transmurality, and distribution of MI injury. Research has shown that CCs can be identified on clinical LGE-MRI (1,3,15,16). However, not all CCs identified on LGE-MRI may be the critical CCs (CCCs) that sustain reentry (1,3,10), which has important implications for infract-related VT ablation.

Computational modeling of individualized hearts reconstructed from LGE-MRI scans has emerged as a platform for noninvasive investigation of heart rhythm disorders; it has been used for risk stratification in patients with MI (17–19), prediction of reentry location (20–23), and recently, to demonstrate the feasibility of simulation-driven VT ablation targeting (24). A personalized model of an MI patient heart allows the visualization and investigation not only of the distribution and morphology of the CCs in the zone of infarct but also the determination of the 3D characteristics of conduction through the CCCs that sustain VT(s) in the given patient. The objective of this study was to use an LGE-MRI-based personalized virtual-heart modeling approach (17) in a retrospective cohort of six MI patients with VT to 1) identify the CCCs, 2) provide a mechanistic understanding of how different VT morphologies are sustained in these patients, 3) investigate the role of the CCC structural features in VT maintenance, and 4) relate the 3D CCC structure and conduction to the ablation strategy for the given VT. An improved knowledge of the characteristics of propagation through the CCCs in the zone of infarct is important for designing optimal ablation strategies for infarct-related VT.

MATERIALS AND METHODS

LGE-MRI images of six patients with MI and spontaneous stable monomorphic VT before the MRI were used in this study for model construction. The same heart models were used in a recent study examining the potential of personalized virtual-heart technology for guiding ablation of infarct-related VT (part of retrospective cohort without implantable cardioverter defibrillator) (24). Ablation targets in that study were determined with an automatic algorithm based on flow networks, precluding the inquiry into CC structures and their relation to induced VTs. The six patient scans were chosen here on the basis of the availability of clinical data for comparison and the quality of the clinical LGE-MRI scans, allowing for thorough CC examination, in addition to being from patients with stable monomorphic VT. Full details regarding the patient cohort as well as detailed information regarding model construction can be found in the original study (24). Briefly, the myocardium boundaries were semiautomatically delineated, and regions of gray zone (GZ) (zone of intermediate intensity on LGE-MRI), core scar, and noninfarcted tissue were segmented from the clinical LGE-MRI by means of signal thresholding (25). Tetrahedral meshes were constructed directly from the segmented images using a previously described approach (26). Fiber orientations in the mesh were assigned using a validated rule-based method (27).

Electrophysiological properties were assigned in the model as previously described in full detail (24). Briefly, core scar was modeled as insulator. Noninfarcted tissue and GZ were assigned human ventricular myocyte action potential kinetics, with the latter having remodeled ionic current properties. The mathematical description of electrical conduction in cardiac tissue was based on the monodomain representation. Conductivity values in the model were assigned such that resultant conduction velocities were close to those measured clinically, as described in Prakosa et al. (24).

A rapid pacing protocol was used to induce VT in the six models, as described previously (17,19,24). The protocol consisted of six beats (S1) at a cycle length of 600 ms followed by a premature stimulus (S2) initially given at 90% of the S1 cycle length. The timing between S1 and S2 was progressively shortened until reentry was induced. If reentry was not induced, a second premature stimulus (S3) was delivered after S2. If VT was still not induced, a third premature stimulus (S4) was delivered after S3. 5 s of VT were simulated.

For each VT morphology induced in the models, the reentrant circuit was identified through the analysis of the 3D reentrant wave propagation. Multiplane analysis of the monomorphic VT reentrant behavior in the 3D ventricle over the duration of the simulation identified the CCC(s) sustaining each VT. After CCC identification, 3D in silico ablation with a 3.5 mm single-point ablation radius (corresponding to the extent of a single clinical lesion (28)), in which the tissue in the lesion was rendered as a scar in the model, was performed at an optimal part of the CCC. The simulations were then repeated to demonstrate postablation VT noninducibility. Finally, the ablation targets predicted in our model were compared with the corresponding ablation lesions executed in the clinic.

The resolution of the clinical MRI images used in this study is $1.5 \times 1.5 \times 10$ mm. As the out-of-plane resolution was insufficient to adequately resolve the channel width, we analyzed only CCs the width of which could be analyzed in the in-plane direction only. The width of the channel here refers to the minimal diameter, at any point along the channel (rather, at any point of the channel that belongs to an MRI short-axis slice), of the local sphere that fits tightly between the barriers surrounding the CC. For anatomical reentry ("I" and "T" type) in 3D, the epicardium or endocardium often bound two sides of the channel, as shown in the left panel in Fig. 1. The rest of the channel boundary is composed of core scar. Fig. 1 shows one example of "I" type channel, which is on one side bounded by the epicardium, and the rest of the channel boundary is core scar (scar in the subendocardium in green, and scar in the two lateral directions in yellow). For functional reentry, the CC width is defined the same way, with the difference that on one side, the channel is bounded by functional block rather than scar.

RESULTS

Table 1 summarizes the volumes of noninfarcted myocardium, GZ, and core scar in the reconstructed heart models for the six patients. The mean ventricular volume was 143.8 cm^3. The percentage, by volume, of noninfarcted myocardium within the ventricles ranged from 58.7 to 92.8%, whereas the percentage by volume of GZ and core scar had a range of 5.5–35.6% and 1.1–34.4%, respectively. There were 1–4 VT morphologies (2.7 ± 1.2) induced in each model, sustained by propagation through CCCs. There were other CCs in the models as well, but those were conduits of propagation during VT and not critical structures

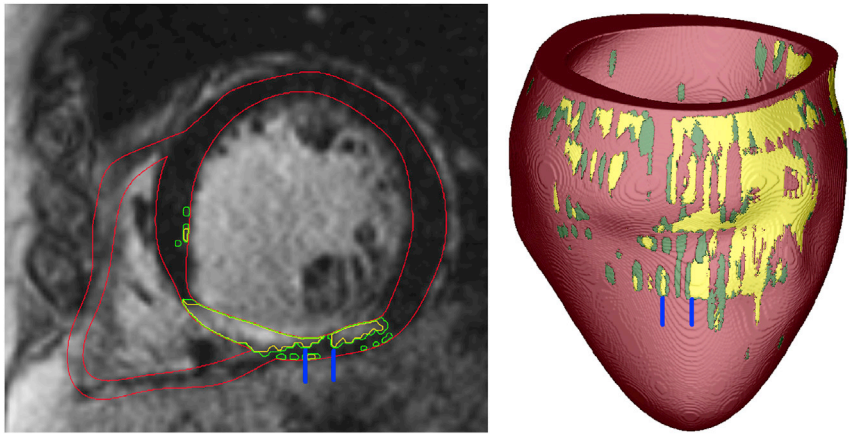

FIGURE 1 Left: a slice of an MRI image of one model. Red lines are the segmented ventricular boundaries, yellow lines are the segmented boundaries of core scar, and green lines are the segmented boundaries of the GZ. Right: the corresponding reconstructed model is shown. Blue lines demarcate the channel manifestation on the epicardial surface. To see this figure in color, go online.

of VT maintenance. Of all VTs induced in the patient-specific models, 63% were sustained by reentries through CCCs surrounded by scar on all sides (Fig. 2, left and middle images), whereas the remaining VTs (37%) involved rotational activity around an area of functional block (Fig. 2, right images). In all cases, the CCCs consisted of GZ tissue (Fig. 2). Below, we present the general mechanistic findings about the different CCCs sustaining VTs in the models, and then we illustrate these findings with specific simulation examples.

In the first type of VTs (i.e., those involving CCCs surrounded by scar on all sides), the CCCs were two types, either "I" or "T" type (shown schematically in two dimensions (2D) in Fig. 2), which accounted for 43.8 and 18.8% of the VT morphologies in all patients, respectively. The I-type CCC involved a single 3D pathway, often of convoluted shape. In the T-type CCC (also referred to as Y-type), the wavefront propagated through a 3D channel that split into two (often unequal) branches, all bounded by nonconducting scar. As illustrated in the examples below, VT morphology through the I- or T-type CCCs could be either figure-of-eight or circular reentry, depending of the 3D structure of the specific CCC. The predominant VT morphologies associated with the I and T CCCs are indicated schematically by the white arrows in Fig. 2. In each case the VT morphology, whether figure-of-eight or circular, depended on the presence or absence, respectively, of symmetry in the 3D structure of the CCC. T-type CCCs were more likely to be asymmetrical, resulting in the predominance of circular reentries in these cases.

In the third type of VT (functional reentry), rotational activity was around an area (3D surface) of functional block between GZ and noninfarcted tissue (shown schematically in 2D by the black line in Fig. 2, right), formed because noninfarcted tissue was refractory at the time of wave propagation through the slower-conducting GZ. The 3D functional block surface could enclose a CCC from all sides (an entirely functional reentry VT) or only partially, as one side of the CCC could be bounded by scar (partially functional reentry VT, as in Fig. 2, right). In the latter case, the reentry was not entirely functional. Again, asymmetry of the CCC boundaries was the determinant factor in the type of reentry; in the cases found in our simulations, all reentries were circular (shown schematically in 2D by the white arrows in Fig. 2, right).

Fig. 2 depicts also schematically, in 2D, the in silico ablation strategy in the models. We performed ablations at optimal locations within the CCCs, which were the narrowest portions of the I-type or functional reentry CCCs, and the locations of branching of the T-type CCCs. The widths of the CCCs at the locations of ablation for all VTs and in all patients is presented in Table 1; the mean width was

TABLE 1 The Volumes of the Reconstructed Heart Models and Predicted Channel Characteristics

Model	Noninfarct (cm^3)	% of Total Volume	GZ (cm^3)	% of Total Volume	Core Scar (cm^3)	% of Total Volume	Narrowest Channel Width (mm)	Channel Types (% of Total Channel Numbers)			Ablation (cm^3)
								I	T	F	
P01	115.9	85.4	10.5	7.7	9.3	6.9	9.0 ± 2.8	0	1	3	0.58
P02	114.6	78.0	6.0	4.1	26.4	17.9	10.7 ± 2.1	2	1	0	0.286
P03	133.1	92.8	9.2	6.4	1.1	0.8	6.6 ± 0.6	0	0	2	0.910
P04	98.7	58.7	35.6	21.2	33.8	20.1	14.9	0	0	1	0.417
P05	106.7	64.5	24.3	14.7	34.4	20.8	8.8 ± 4.0	3	1	0	0.395
P06	84.5	82.1	5.5	5.3	12.9	12.6	11.8 ± 6.9	2	0	0	0.194
Mean ± SD	108.9 ± 16.6	76.9 ± 12.9	15.2 ± 12.1	9.9 ± 6.7	19.7 ± 13.9	13.2 ± 8.0	9.7 ± 3.6	7 (43.8)	3 (18.8)	6 (37.4)	0.46 ± 0.25

F, GZ-mediated functional reentry; I, "I" type channel; T, "T" type channel.

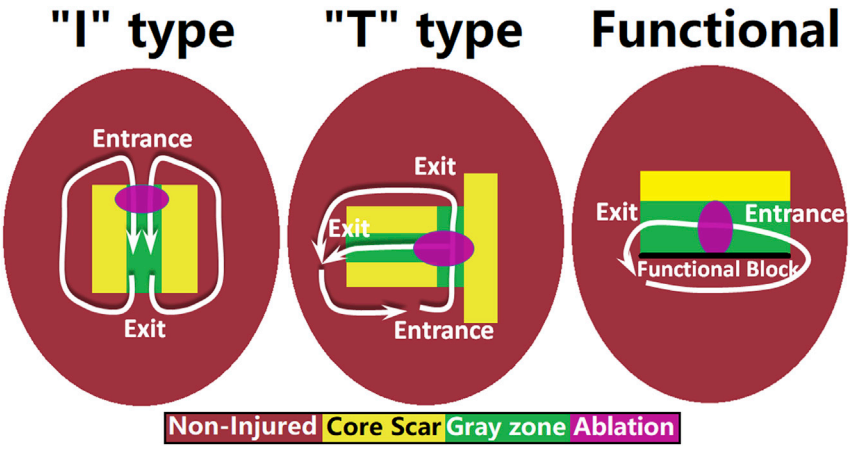

FIGURE 2 Schematic diagram of the three types of VTs sustained by propagation through a CCC. Different colors represent different tissue types: noninjured (*red*), core scar (*yellow*), and GZ (*green*). The white arrows show the predominant direction of reentrant wave propagation for each type of CCC as found in our simulations. The black line in the functional reentry schematic represents conduction block. The optimal ablation lesion that terminated each type of reentry is shown schematically in purple. To see this figure in color, go online.

9.7 ± 3.6 mm. Simulated ablation at these optimal sites terminated the corresponding VTs in all patients. The mean total ablation lesion volume per patient was 460 mm^3.

Below are specific examples illustrating these findings. Fig. 3 shows simulations from a patient-specific model in which two VT morphologies were sustained by propagation through I-type CCCs. The GZ and core scar in the model were mainly distributed in the septum and posterior wall (Fig. 3 *A*). The first VT induced in this model had a figure-of-eight morphology with a CCC (made up of GZ) and located on the septum close to the anterior wall; there were other CCs in the model as well, which were passive conduits of propagation during VT. The second VT and its CCC in this patient heart (Fig. 3 *B*) were located at the posterior middle wall of the left ventricle (LV); VT morphology was circular. Simulated ablation of the narrowest region in the CCCs terminated the corresponding reentries. The predicted ablation targets matched well the clinical lesions, as shown in the fourth panels of Fig. 3, *A* and *B*.

Fig. 4 illustrates two patient heart models each presenting with a VT with T-type CCC. The top model has GZ and core scar distributed mainly in the septum and posterior wall.

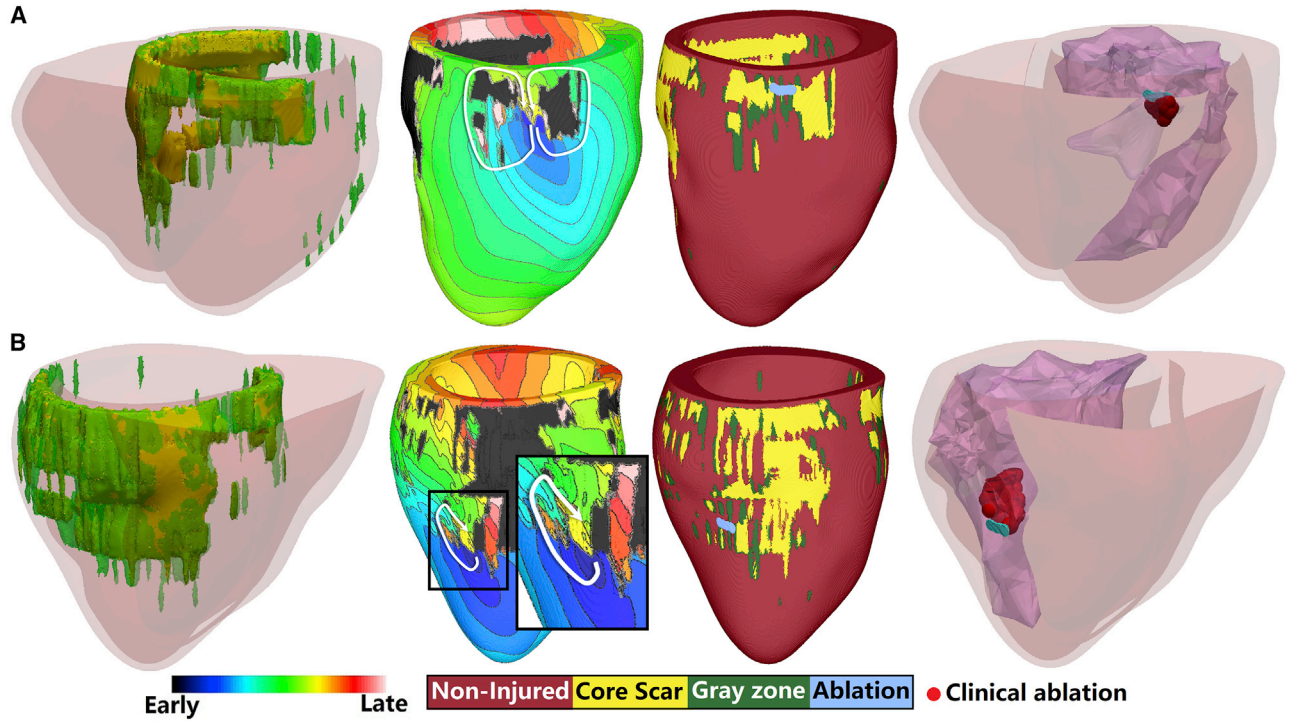

FIGURE 3 Two examples of "I" type channel-based reentry in one patient. The first column shows the model geometry, which includes both LV and right ventricle. The second column shows the activation map of each reentry in the LV. The third column shows the geometry of only the LV and the predicted ablation lesion for the corresponding reentry. The last column shows the ablation targets predicted (*blue*) and the clinical ablation lesions (*red*). The color scale indicates activation times for column 2. To see this figure in color, go online.

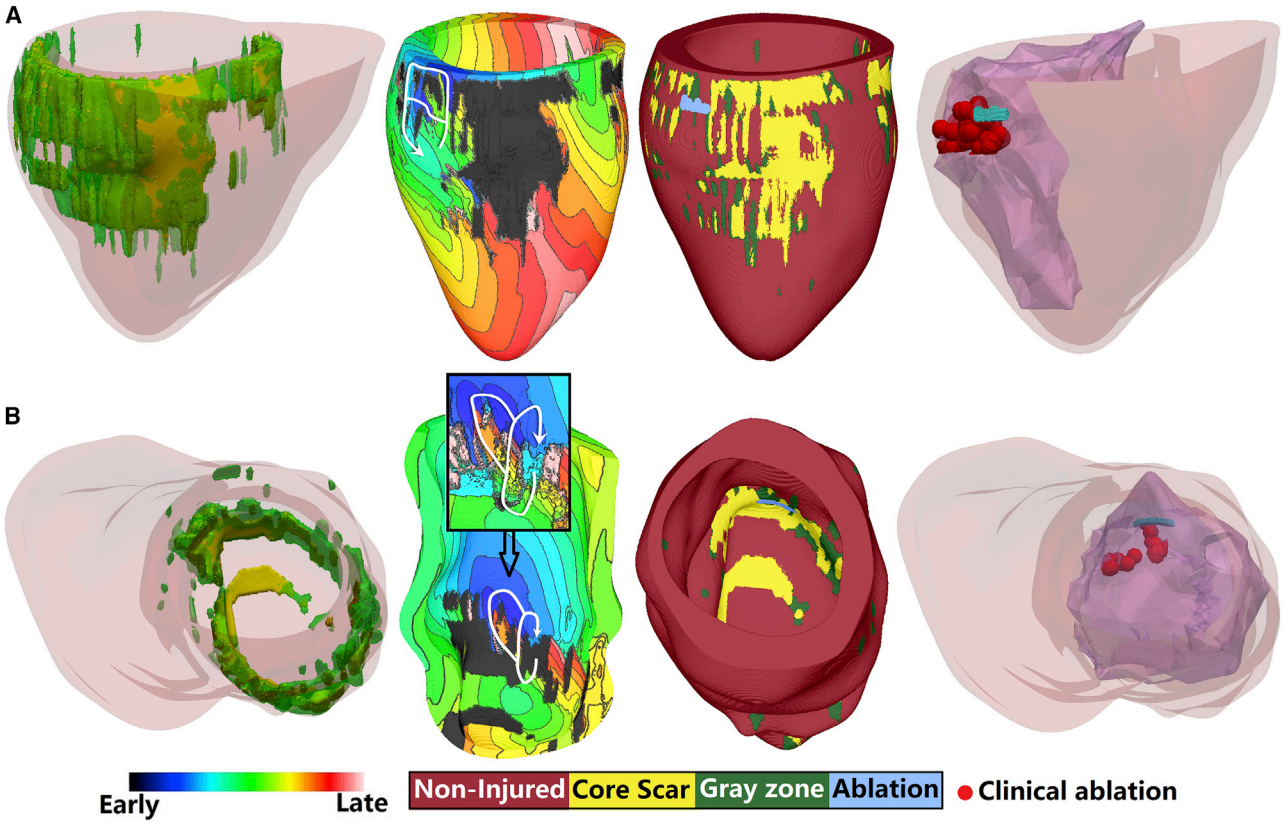

FIGURE 4 Examples of "T" type channel-based reentry in two different patients. The first column shows the biventricular geometry of each model. The second column shows the activation map of each reentry in the LV. The second panel in (*B*) also shows a zoomed-in view of the reentry region with the core scar on the endocardium removed to show the wavefront propagation of the reentry in the myocardium. The third column shows the geometry of only the LV and the predicted ablation lesion for the corresponding reentry. The last column shows the ablation targets predicted in the model (*blue*) and the clinical ablation lesions (*red*). The color scale indicates activation times for column 2. To see this figure in color, go online.

As shown in the second panel of Fig. 4 *A*, the VT was located at the posterior wall close to the LV base and its morphology was circular. In the other example of a VT sustained by propagation through a T-type CCC (Fig. 4 *B*), GZ and core scar in the model were in the LV, and the VT was located on the posterior wall. The morphology of the VT was circular. The in silico ablations at the intersection of the two branches of the T-type CCC terminated the VTs in both models, and the in silico ablation targets corresponded well with the clinical ablation lesions (see fourth panels).

Fig. 5 shows two VTs in the same patient heart model. Both VTs are of the functional reentry type, sustained by propagation through a CCC in the GZ. The first VT (top row) was perpetuated at the posterior wall close to the base. This was an entirely functional reentry VT with circular morphology. The second VT was located on the midposterior wall, further from the base. It was a partially functional reentry VT with a circular morphology, with boundaries of the CCC being functional block and scar on opposing sides. In both cases, ablation of the CCC at the narrowest part between the line of functional block and the boundary formed by either core scar or functional block (Fig. 5, bottom row) on the other side of the channel terminated the reentry. As shown, the predicted in silico ablation targets matched well the clinical ablation lesions. The videos for three functional reentries in three models were also provided (See Videos S1, S2, and S3).

DISCUSSION

Although it is well understood that VT in post-MI patients involve various components of infarct-related structural remodeling, it has been difficult to obtain comprehensive individualized 3D structure-function relationship in regard to VT maintenance in the MI patient heart. This is due to the fact that interrogating the electrical function in the post-MI heart during VT ablation or implantable cardioverter defibrillator implantation involves acquiring information from a single surface or a few pacing locations. Despite the recent advent of higher resolution endocardial mapping (2,5,29), information regarding the relationship between 3D infarct structure and the 3D VT propagation in the infarct-remodeled human heart remains limited.

Constructing personalized computational models of post-MI hearts has recently emerged as a powerful means to

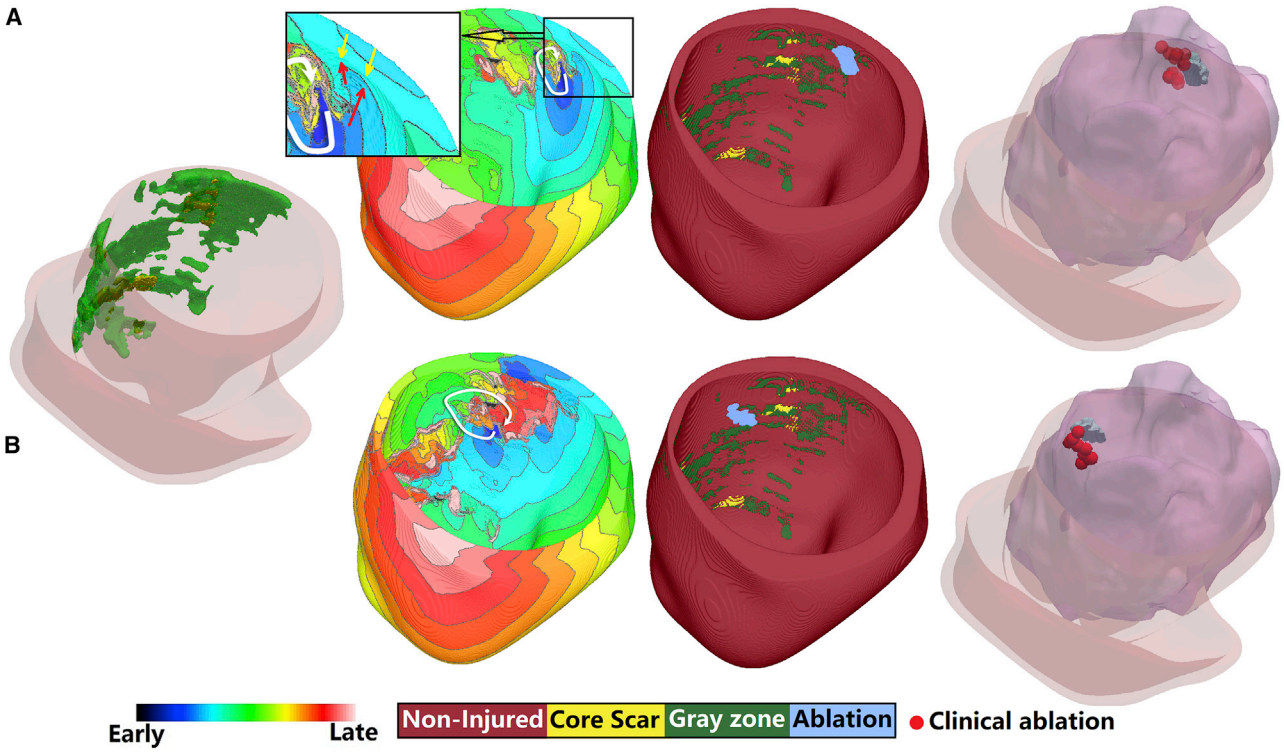

FIGURE 5 Two examples of functional reentry VT in one patient. The first column shows the biventricular model geometry. The second column shows the activation map of each reentry in LV. The third column shows the geometry of only the LV and the predicted ablation lesion for the corresponding reentry. The last column shows ablation targets predicted in the model (*blue*) and the clinical ablation lesions (*red*). The inset in the second panel of the first row illustrates the two activation wavefronts colliding as they propagate from endo- and epicardium. Yellow arrows mark the wavefront propagating from the epicardium, whereas red arrows mark the wavefront advancing from endocardium. The color scale indicates activation times for column 2. To see this figure in color, go online.

reveal the mechanisms of VT maintenance (10,30), establish propensity to VT (i.e., define risk of sudden cardiac death) (17,19), and demonstrate the feasibility of identifying VT ablation targets offline before the ablation procedure (31). In this work, we used our personalized virtual-heart simulation approach to provide enhanced understanding of the types of remodeled structures that are critical for VT maintenance. Specifically, here, we conducted the first 3D assessment of the CCCs sustaining the different VTs in these patients, investigated their types and 3D structural features, and related that structure to the ablation strategy for the given VT. We also characterized the types of reentrant activity associated with the different CCCs. Our results show that 1) the observed reentries in each patient's model were sustained by a limited number (2.7 ± 1.0) of CCCs; 2) three different types of CCCs were identified: "I" type, "T" type, and those associated with functional reentry, giving rise to different VT morphologies; and 3) virtual ablation of the narrowest region in each CCC for I-type or functional reentry VTs or at the point of intersection in the T-type CCC was sufficient to terminate reentry in all models. Among the different types of CCC, the I-type were found to be most prevalent (43.8%). Interestingly, over 37% of VT morphologies were found here to be functional reentries with CCCs bounded by lines of block on one or both sides (i.e., partial or full functional reentry). The T-type CCCs were the least frequent.

Although CCs, which create the substrate for reentry, have been documented in animal models and in ischemic cardiomyopathy patients by endocardial voltage mapping (1,3,4), activation mapping (2,32), or entrainment mapping (2), experimental and clinical studies have also shown that CCs can be identified on LGE-MRI (1,3). The limitation of using LGE-MRI for CCC detection is that there is no established method to determine which CCs are the critical ones that sustain the VTs. Perez-David et al. reported that 58% (15 out of 26) of CCs identified by LGE-MRI were associated with the critical isthmuses of clinical VT. Fernandez-Armenta et al. showed a higher ratio of 74%. In each of our models, we determined, based on analysis of VT simulation results rather than on an algorithm defining what constitutes a channel, the CCCs for each VT. In 87.5% (14 out of 16) of the VTs found in our study, the detected CCCs matched the clinical ablation lesions that terminated the VTs. Furthermore, functional reentry VTs, such as those identified here and also observed by high-resolution recordings (2,29), cannot be determined from imaging alone. That indicates that determining the CCCs with the use of

personalized ventricular models that incorporate both a remodeled structure and electrophysiology might provide higher accuracy than the direct examination of LGE-MRI to detect CCCs.

The characteristics of the I-type CCC identified in our models are consistent with those described in other publications; the channels are bounded by core scar on all sides, and GZ serves as conducting tissue inside the channel (1,3–5). The mean narrowest diameter of the three CCC types found here was 9.7 mm, very close to the value of 7.4 mm reported by Anter et al. (2) in swine and 9.5 mm reported by Martin et al. in patients (5). The CCC width determined from our models has an average value of 9.7 mm. As the boundaries of an I-type CCC were typically asymmetrical and the channel was rarely straight, VT morphologies associated with it ranged from figure-of-eight to circular reentry. The finding for the T-type CCC was similar in regard to the VT morphologies it could sustain; unequal branch length, different branch geometries, and asymmetries also resulted in VTs of different patterns, from figure-of-eight to circular of different circuit lengths and shapes.

We recently conducted a sensitivity study of the effect of electrophysiological parameter variability on reentry morphology and VT location (33). The simulation results demonstrated that the VT ablation target uncertainty in patient-specific ventricular models with an average representation of VT-remodeled electrophysiology is relatively low, and the ablation target locations remain the same as the localization of the induced VTs was primarily driven by the remodeled structural substrate. The conclusions from the study were that although electrophysiological parameters variation had some effects on reentry morphology and location, our models with average electrophysiology parameters could predict the vast majority of the reentries recorded in the clinic. This conclusion was the same even for cases when even there was a functional reentry aspect in the VT as even in this case, the structural contribution to VT location remains strong.

This study is the, to our knowledge, first to characterize the functional reentry VTs and their relation to the surrounding scar. Although two previous studies have mentioned the presence of functional lines of block, one experimental (2) and one a clinical study in patients with MI (5), the actual contribution of the surrounding scar could not be examined as no imaging was performed. Interestingly, over one third of the VTs found here were either partially functional or entirely functional reentries; in the latter cases, CCC boundaries were functional lines of block (i.e., surfaces of block in 3D). This is consistent with the report that the identified regions of functional block in patients accounted for 30% of all conduction barriers (5). Another important finding in this study is that all CCCs, regardless of type, consist of GZ tissue, the latter proving the substrate for slow propagation. This fact, although not well appreciated in clinical research, is consistent with experimental and clinical findings (34,35).

Finally, in our models, ablating an average total volume of 460 mm^3 per patient in the narrowest regions (for T-type CCCs, this is the intersection region) of the CCCs terminated all VTs. Lesions executed in the clinic to terminate postinfarction VT typically encompass much larger areas of tissue (an average volume of 4270 mm^3). Ablating at the narrowest part of a CCC or at the branch crossing of a T-type CCC resulted in much smaller lesions than a typical clinical lesion. Importantly, our predicted 3D targets were both subendocardial (43.8%) and subepicardial (56.2%). Thus, our simulation approach could inform the clinician whether the predicted targets are endo- or epicardial before the procedure so that adequate preparations could be made as these require different preprocedure set ups, in terms of anticoagulation and other factors.

One limitation of the current study is the small sample size of six patients. Another limitation is that no activation maps were acquired in the clinic, so the VT morphologies detected in our model cannot be directly compared with activation maps. Furthermore, clinical LGE-MRI resolution limits the accuracy of the reconstructed channel geometry in the longitudinal direction.

CONCLUSIONS

The results presented in this article demonstrate that the personalized virtual-heart methodology could be used to obtain insights into human infarct-related VT, providing information about the organization and structure of CCCs that sustain VT, and how the different types of CCCs determine VT morphology. Furthermore, as the ablation targets predicted in our models are consistent with the ablation lesions executed in the clinic, the current study underscores the potential of patient-specific models to identify offline, before the procedure, the CCCs which sustain reentry thus helping to guide the clinical procedure.

SUPPORTING MATERIAL

Supporting Material can be found online at https://doi.org/10.1016/j.bpj.2019.07.024.

AUTHOR CONTRIBUTIONS

D.D., A.P., and P.N. performed LGE-MRI scan segmentation and model creation. D.D. performed simulations of VT in all models. D.D., A.P., and N.A.T. analyzed the data. D.D., J.S., and N.A.T. wrote the manuscript. All authors discussed the results and commented on the manuscript.

ACKNOWLEDGMENTS

N.A.T. acknowledges support from National Institutes of Health (Pioneer Award DP1-HL123271 and grants R01 HL126802 and U01 HL141074) and a grant from Foundation Leducq. D.D. acknowledges support from Dalian University of Technology (DUT18RC(3)068).

REFERENCES

1. Fernándsez-Armenta, J., A. Berruezo, …, J. Brugada. 2013. Three-dimensional architecture of scar and conducting channels based on high resolution ce-CMR: insights for ventricular tachycardia ablation. *Circ. Arrhythm. Electrophysiol.* 6:528–537.
2. Anter, E., C. M. Tschabrunn, …, M. E. Josephson. 2016. High-resolution mapping of postinfarction reentrant ventricular tachycardia: electrophysiological characterization of the circuit. *Circulation.* 134:314–327.
3. Perez-David, E., A. Arenal, …, F. Fernández-Avilés. 2011. Noninvasive identification of ventricular tachycardia-related conducting channels using contrast-enhanced magnetic resonance imaging in patients with chronic myocardial infarction: comparison of signal intensity scar mapping and endocardial voltage mapping. *J. Am. Coll. Cardiol.* 57:184–194.
4. Estner, H. L., M. M. Zviman, …, H. R. Halperin. 2011. The critical isthmus sites of ischemic ventricular tachycardia are in zones of tissue heterogeneity, visualized by magnetic resonance imaging. *Heart Rhythm.* 8:1942–1949.
5. Martin, R., P. Maury, …, F. Sacher. 2018. Characteristics of scar-related ventricular tachycardia circuits using ultra-high-density mapping. *Circ. Arrhythm. Electrophysiol.* 11:e006569.
6. Zhong, H., J. M. Lacomis, and D. Schwartzman. 2007. On the accuracy of CartoMerge for guiding posterior left atrial ablation in man. *Heart Rhythm.* 4:595–602.
7. Brugada, J., A. Berruezo, …, L. Mont. 2003. Nonsurgical transthoracic epicardial radiofrequency ablation: an alternative in incessant ventricular tachycardia. *J. Am. Coll. Cardiol.* 41:2036–2043.
8. Sosa, E., M. Scanavacca, …, J. A. Ramires. 2000. Nonsurgical transthoracic epicardial catheter ablation to treat recurrent ventricular tachycardia occurring late after myocardial infarction. *J. Am. Coll. Cardiol.* 35:1442–1449.
9. Dong, J., D. Dalal, …, H. Calkins. 2007. Impact of heart rhythm status on registration accuracy of the left atrium for catheter ablation of atrial fibrillation. *J. Cardiovasc. Electrophysiol.* 18:1269–1276.
10. Pashakhanloo, F., D. A. Herzka, …, N. A. Trayanova. 2018. Role of 3-dimensional architecture of scar and surviving tissue in ventricular tachycardia: insights from high-resolution ex vivo porcine models. *Circ. Arrhythm. Electrophysiol.* 11:e006131.
11. de Bakker, J. M., F. J. van Capelle, …, R. N. Hauer. 1988. Reentry as a cause of ventricular tachycardia in patients with chronic ischemic heart disease: electrophysiologic and anatomic correlation. *Circulation.* 77:589–606.
12. Peters, N. S., and A. L. Wit. 1998. Myocardial architecture and ventricular arrhythmogenesis. *Circulation.* 97:1746–1754.
13. Ashikaga, H., T. Sasano, …, H. R. Halperin. 2007. Magnetic resonance-based anatomical analysis of scar-related ventricular tachycardia: implications for catheter ablation. *Circ. Res.* 101:939–947.
14. Nakahara, S., M. Vaseghi, …, K. Shivkumar. 2011. Characterization of myocardial scars: electrophysiological imaging correlates in a porcine infarct model. *Heart Rhythm.* 8:1060–1067.
15. Andreu, D., A. Berruezo, …, J. Brugada. 2011. Integration of 3D electroanatomic maps and magnetic resonance scar characterization into the navigation system to guide ventricular tachycardia ablation. *Circ. Arrhythm. Electrophysiol.* 4:674–683.
16. Andreu, D., J. T. Ortiz-Pérez, …, A. Berruezo. 2015. 3D delayed-enhanced magnetic resonance sequences improve conducting channel delineation prior to ventricular tachycardia ablation. *Europace.* 17:938–945.
17. Arevalo, H. J., F. Vadakkumpadan, …, N. A. Trayanova. 2016. Arrhythmia risk stratification of patients after myocardial infarction using personalized heart models. *Nat. Commun.* 7:11437.
18. Vadakkumpadan, F., N. Trayanova, and K. C. Wu. 2014. Image-based left ventricular shape analysis for sudden cardiac death risk stratification. *Heart Rhythm.* 11:1693–1700.
19. Deng, D., H. J. Arevalo, …, N. A. Trayanova. 2016. A feasibility study of arrhythmia risk prediction in patients with myocardial infarction and preserved ejection fraction. *Europace.* 18 (*Suppl 4*):iv60–iv66.
20. Deng, D., H. Arevalo, …, N. Trayanova. 2015. Accuracy of prediction of infarct-related arrhythmic circuits from image-based models reconstructed from low and high resolution MRI. *Front. Physiol.* 6:282.
21. Ashikaga, H., H. Arevalo, …, H. R. Halperin. 2013. Feasibility of image-based simulation to estimate ablation target in human ventricular arrhythmia. *Heart Rhythm.* 10:1109–1116.
22. Zahid, S., H. Cochet, …, N. A. Trayanova. 2016. Patient-derived models link re-entrant driver localization in atrial fibrillation to fibrosis spatial pattern. *Cardiovasc. Res.* 110:443–454.
23. Zahid, S., K. N. Whyte, …, N. A. Trayanova. 2016. Feasibility of using patient-specific models and the "minimum cut" algorithm to predict optimal ablation targets for left atrial flutter. *Heart Rhythm.* 13:1687–1698.
24. Prakosa, A., H. J. Arevalo, …, N. A. Trayanova. 2018. Personalized virtual-heart technology for guiding the ablation of infarct-related ventricular tachycardia. *Nat. Biomed. Eng.* 2:732–740.
25. Prakosa, A., P. Malamas, …, F. Vadakkumpadan. 2014. Methodology for image-based reconstruction of ventricular geometry for patient-specific modeling of cardiac electrophysiology. *Prog. Biophys. Mol. Biol.* 115:226–234.
26. Prassl, A. J., F. Kickinger, …, G. Plank. 2009. Automatically generated, anatomically accurate meshes for cardiac electrophysiology problems. *IEEE Trans. Biomed. Eng.* 56:1318–1330.
27. Bayer, J. D., R. C. Blake, …, N. A. Trayanova. 2012. A novel rule-based algorithm for assigning myocardial fiber orientation to computational heart models. *Ann. Biomed. Eng.* 40:2243–2254.
28. Narayan, S. M., D. E. Krummen, …, J. M. Miller. 2012. Treatment of atrial fibrillation by the ablation of localized sources: CONFIRM (Conventional Ablation for Atrial Fibrillation With or Without Focal Impulse and Rotor Modulation) trial. *J. Am. Coll. Cardiol.* 60:628–636.
29. Anter, E., A. G. Kleber, …, A. E. Buxton. 2018. Infarct-related ventricular tachycardia: redefining the electrophysiological substrate of the isthmus during sinus rhythm. *JACC Clin. Electrophysiol.* 4:1033–1048.
30. Arevalo, H., G. Plank, …, N. Trayanova. 2013. Tachycardia in post-infarction hearts: insights from 3D image-based ventricular models. *PLoS One.* 8:e68872.
31. Prakosa, A., H. J. Arevalo, …, N. A. Trayanova. 2018. Personalized virtual-heart technology for guiding the ablation of infarct-related ventricular tachycardia. *Nat. Biomed. Eng.* 2:732–740.
32. Ciaccio, E. J., H. Ashikaga, …, J. Coromilas. 2007. Model of reentrant ventricular tachycardia based on infarct border zone geometry predicts reentrant circuit features as determined by activation mapping. *Heart Rhythm.* 4:1034–1045.
33. Deng, D., A. Prakosa, …, N. A. Trayanova. 2019. Sensitivity of ablation targets prediction to electrophysiological parameter variability in image-based computational models of ventricular tachycardia in post-infarction patients. *Front. Physiol.* 10:628.
34. de Bakker, J. M., F. J. van Capelle, …, J. R. Lahpor. 1993. Slow conduction in the infarcted human heart. 'Zigzag' course of activation. *Circulation.* 88:915–926.
35. Tschabrunn, C. M., S. Roujol, …, E. Anter. 2016. A swine model of infarct-related reentrant ventricular tachycardia: electroanatomic, magnetic resonance, and histopathological characterization. *Heart Rhythm.* 13:262–273.